

# Spalling Experiments on Large Hard Rock Specimens

Lars Jacobsson · Karin Appelquist ·  
Jan Erik Lindkvist

Received: 21 November 2013 / Accepted: 15 September 2014 / Published online: 7 October 2014  
© Springer-Verlag Wien 2014

**Abstract** Specimens of coarse-grained Äspö diorite were axially compressed to observe stress-induced spalling. The specimens had a novel design characterized by two manufactured large radius notches on opposite sides. The tangential stress occurring in the notches aimed to represent the tangential loading around a circular opening. Fracture stages were monitored by acoustic emission measurements. Rock chips were formed similar to those found in situ, which indicates a similar fracture process. Slabs were cut out from the specimens and impregnated using a fluorescent material to visualize the cracks. The cracks were subsequently examined by the naked eye and by means of microscopy images, from which fracture paths could be identified and related to different minerals and their crystallographic orientations. The microscopy analyses showed how the stress field and the microstructure interact. Parallel cracks were formed 2–4 mm below the surface, sub-parallel to the direction of the maximum principal stress. The crack initiation, the roles of minerals such as feldspar, biotite and quartz and their grain boundaries and crystallographic directions are thoroughly studied and discussed in this paper. Scale effects, which relate to the stress gradient and microstructure, are discussed.

**Keywords** Crystalline rock · Spalling · Laboratory experiments · Microscopy analysis · Fractures

## List of symbols

$E$	Young's modulus
$\nu$	Poisson ratio
$\sigma_{ci}$	Crack initiation stress
$\sigma_{cd}$	Crack damage stress
UCS	Uniaxial compressive strength
$\rho$	Wet density

## 1 Introduction

A large amount of research aiming at an increased understanding of rock spalling has been undertaken since it was first observed in tunnels or in boreholes when subjected to high in situ stress field. Besides observations in tunnels, the spalling phenomenon in crystalline rock or rock-like materials was studied by designated laboratory experiments such as loaded rock blocks containing a central cylindrical hole, in this paper denoted as “hole-in-the-block” tests (e.g. Hoek 1965; Lajtai 1972; Mastin 1984; Haimson and Herrick 1986; Carter et al. 1991; Carter 1992; Martin 1993; Haimson 2007) and hollow cylinder tests (e.g. Daemen and Fairhurst 1971; Gay 1973; Kelsall et al. 1982; Ewy and Cook 1990; Fuenkajorn and Daemen 1992; Myer et al. 1992). Other laboratory tests with the aim to study rock spalling are e.g. plane strain test under biaxial compression on sandstone (Labuz et al. 1996), bending of a compressed beam of synthetic rock (Cho et al. 2010) and eccentric uniaxial compression loading of a granite block (Pinto and Fonseca 2013). Moreover, in situ experiments were carried out in conjunction with nuclear waste repository design (e.g. Mine-by Experiments in Canada, Read and Martin 1996; Martin et al. 1997; Read 2004, Äspö pillar stability experiments, APSE, in Sweden, Andersson 2007).

---

L. Jacobsson (✉)  
Structural and Solid Mechanics, SP Technical Research  
Institute of Sweden, Box 857, 501 15 Borås, Sweden  
e-mail: lars.jacobsson@sp.se

K. Appelquist · J. E. Lindkvist  
Swedish Cement and Concrete Research Institute,  
c/o SP, Box 857, 501 15 Borås, Sweden

It is desirable to correlate stress at the onset of spalling in situ to results from simple and relatively inexpensive laboratory experiments. Since spalling occurs at a surface subjected to large tangential stress, natural attempts have been made to find correlations of the fracturing in specimens subjected to compression such as in the uniaxial compression strength (UCS) test to the field behaviour. It was already observed by Brace et al. (1966) that the onset of crack initiation relates to the volumetric response when deviating from the linear elastic response curve. Various methods to determine the onset of crack initiation using the UCS test have been proposed, such as volumetric strain methods, lateral strain methods and acoustic emission method (cf. review by Nicksiar and Martin 2012). The methods to determine the crack initiation stress from UCS tests yield somewhat different results. Typical values of the crack initiation stress to UCS ratio are 0.35–0.55 for granites and granodiorite (e.g. Eberhardt et al. 1998; Diederichs et al. 2004; Andersson 2007). This can be compared with estimated values of the spalling initiation stress to UCS ratio at in situ experiments, as summarized by Martin and Christiansson (2009), for the Mine-by Experiment (0.56 for Lac Du Bonnet Granite and 0.65 for granodiorite) and in the APSE (0.58 for Äspö diorite).

The results from the hole in the block tests for different diameters show that the tangential stress at the onset of cracking (spalling) depends on the hole diameter. For example tests on Lac du Bonnet granite showed that the ratio of tangential stress to UCS at failure went from 2.6 at 5 mm diameter holes, 1.4–1.6 at 20 mm holes to 0.99–1.2 at 103 mm holes (Martin 1993). This is consistent with other results on limestone where the ratio of tangential stress to UCS decreases for increasing diameter: 2.45 (6.4 mm) to 1.50 (62 mm), (Carter 1992) and 2.62 (22 mm) to 0.81 (110 mm), (Haimson and Herrick 1989). It was for example suggested by Carter (1992) and Martin et al. (1994) that the dependence of hole diameter is a scale and stress gradient effect.

Martin (1997) summarized results from laboratory experiments and in situ investigations on Lac du Bonnet granite. It could be seen that the ratio of tangential stress to UCS was smaller for the in situ experiments than for the corresponding laboratory tests for the same hole diameter (75–100 mm). The discrepancy can be attributed to 3D-stress effects, a relatively high loading rate in the laboratory experiments as compared with the in situ case and stress rotation during excavation that induce damage (Read 2004). The modelling work by Eberhardt (2001) and Diederichs et al. (2004) supports that stress rotation during excavation near the tunnel face induce damage in the rock. Other contributing factors are induced damage on the surface from drilling or excavation due to mechanical forces and heating and local surface irregularities providing

stress concentrations and possible initiation locations (see e.g. Daemen and Fairhurst 1971; Weed and Durham 1982; Autio 1997; Valley and Evans 2005).

It is known that the rock microstructure (grain size distribution, mineral types, pre-existing microcracks) influence the mechanical properties of the rock. Examples of studies where load-induced fracture development in crystalline rock were discussed in relation to the microstructural components and mineralogy are Wong (1982), Kranz (1983), Lajtai (1998), Eberhardt et al. (1999b), Åkesson et al. (2001), Seo et al. (2002), Li et al. (2003), Liu et al. (2006), Lindqvist et al. (2007), Mahabadi (2012).

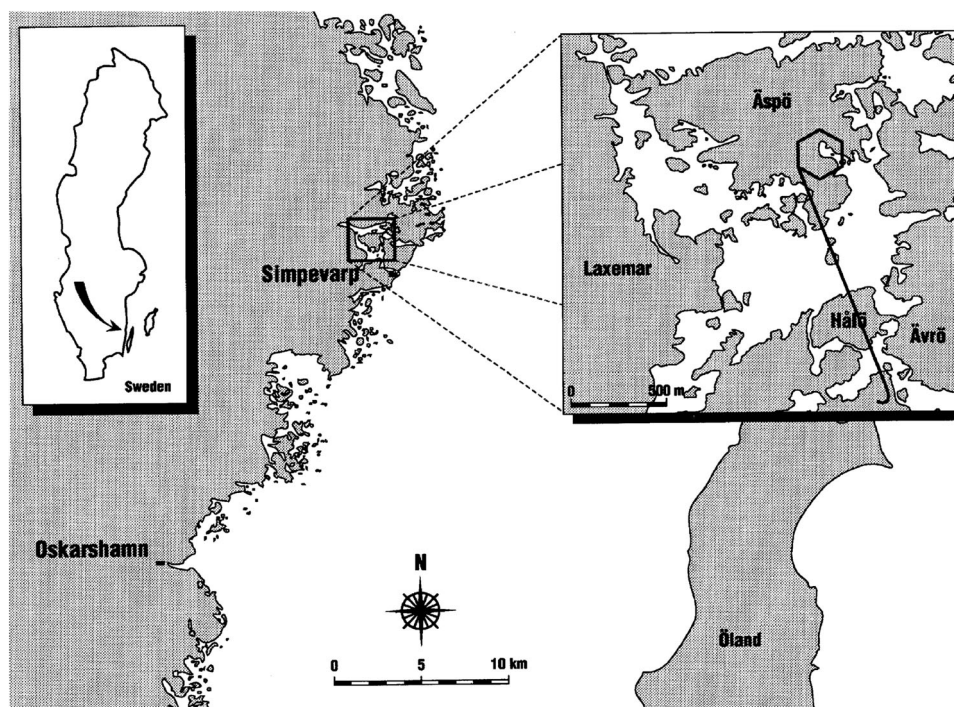
In this paper we present a new test procedure, where a combination of strain and acoustic emission (AE) measurements and visual observations are used to assess the stress at different fracture stages associated with the spalling process around circular openings of a large diameter. The specimens of Äspö diorite used in the tests have an hourglass shape that resemble the wall in underground circular openings. The main measurement is the AE recording, which enables monitoring of the fracture stages. Together with the visual post-examination of the cracks, it gives a detailed insight into the fracture process. The strain measurements were used mainly to verify the FE-model which was used to calculate the stress field in the notches. The strain gauges were able to register evidence of fracturing at a late stage. The visual observations of these tests were restricted to inspections of the specimens after testing, since the area close to the specimen was sealed off due to safety.

The curved surfaces on the sides of the specimens yield a stress concentration and a localization of spalling to the centre of the notch, which are advantageous for the test monitoring and the post-examination of the samples. The main results of the mechanical tests were briefly reported by Jacobsson et al. (2010). In this paper, we present additional results and details from the tests; in particular, an examination of the crack paths in relation to the mineral structure. This type of information of the failure process is fundamental for the understanding and numerical modelling of failure processes when the microstructure is modelled at a grain scale.

One advantage of practical nature with the specimen geometry presented herein, as compared with the hole-in-the-block tests, is that the specimen size can be made smaller when spalling for a given radius (hole diameter) is investigated. Hence, specimens with a larger radius could be tested within available laboratory equipment. This is advantageous since the radius for in situ applications is in general large.

The outline of the paper is as follows: a geological description of the rock is given in Sect. 2. In Sect. 3, the experimental methods used for the mechanical tests and the

**Fig. 1** Location of the Äspö island and the Äspö Hard Rock Laboratory (picture courtesy of SKB)



crack investigations around the spalling areas are described. The results from the mechanical tests are presented in Sect. 4, and Sect. 5 contains the results from the microscopy investigations and crack analyses. The paper ends with a discussion in Sect. 6 and conclusions in Sect. 7.

## 2 Materials: Geology

The analysed specimens are composed of heterogeneous reddish grey, medium-grained, foliated granitoid to quartz monzodioritic rocks belonging to the 1.8 Ga (billion years old) Äspö diorite suite (Kornfält et al. 1997) of the Transscandinavian Igneous Belt (TIB; Gaál and Gorbatschev 1987; Patchett et al. 1987). Samples were collected from the wall in the TASS tunnel at 450 m level at the Äspö Hard Rock Laboratory located in the Simpevarp subarea on the Swedish East Coast (Figs. 1, 2). The definitions (Fig. 3) are based on earlier mapping and analyses of the rock types on the island of Äspö, see Hardenby and Sigurdsson (2010), Berglund et al. (2003) and references in these publications. Due to conflicting data and lack of high resolution lithological data, newer models of the lithology at Äspö are lacking (cf. Berglund et al. 2003). Following the old definitions, the main rock type in the TASS-tunnel is Äspö diorite and varieties of it, although minor occurrences of fine-grained granite, pegmatite, quartz veins/lenses or irregular minor bodies, undifferentiated mafic rocks and hybrid rock occur

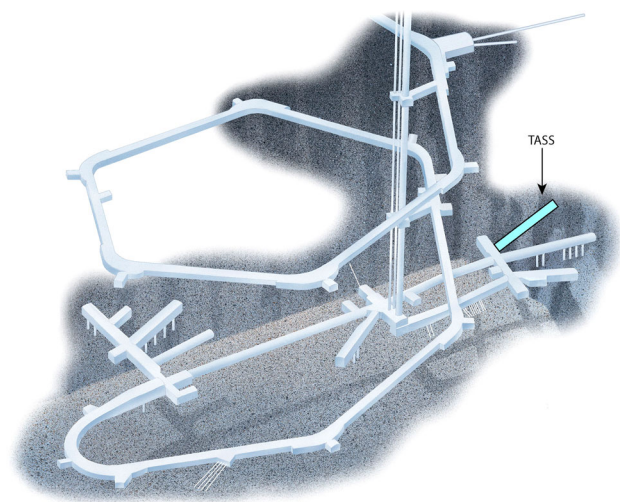


**Fig. 2** Tunnel layout at Äspö Hard Rock Laboratory showing the TASS tunnel (picture courtesy of SKB)

(Hardenby and Sigurdsson 2010). Previous analyses of the Äspö diorite show that the composition of the rock suite ranges from granite to gabbro although most analyses fall in the granodiorite to quartz monzodiorite field of the Streckeisen diagram (Fig. 4).

The analysed rock contains plagioclase, K-feldspar, quartz, biotite, epidote, and accessory amphibole, sphene, chlorite, apatite, calcite and opaque minerals. Large feldspar megacrysts up to 30 mm size are abundant in the rock.

**Fig. 3** Bedrock map of the Äspö island (picture courtesy of SKB)

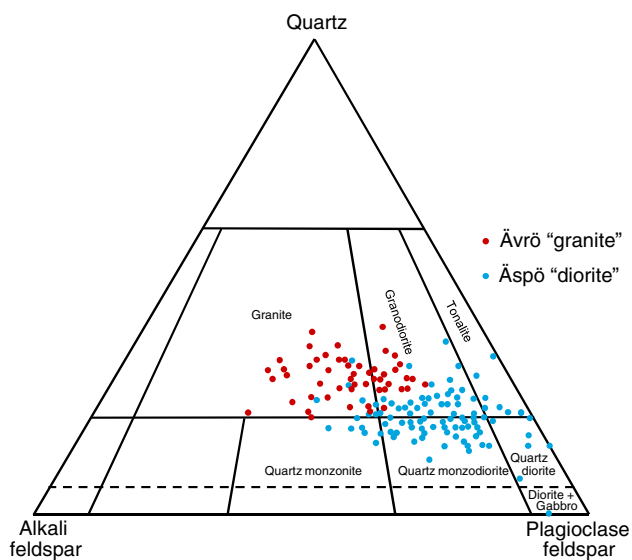
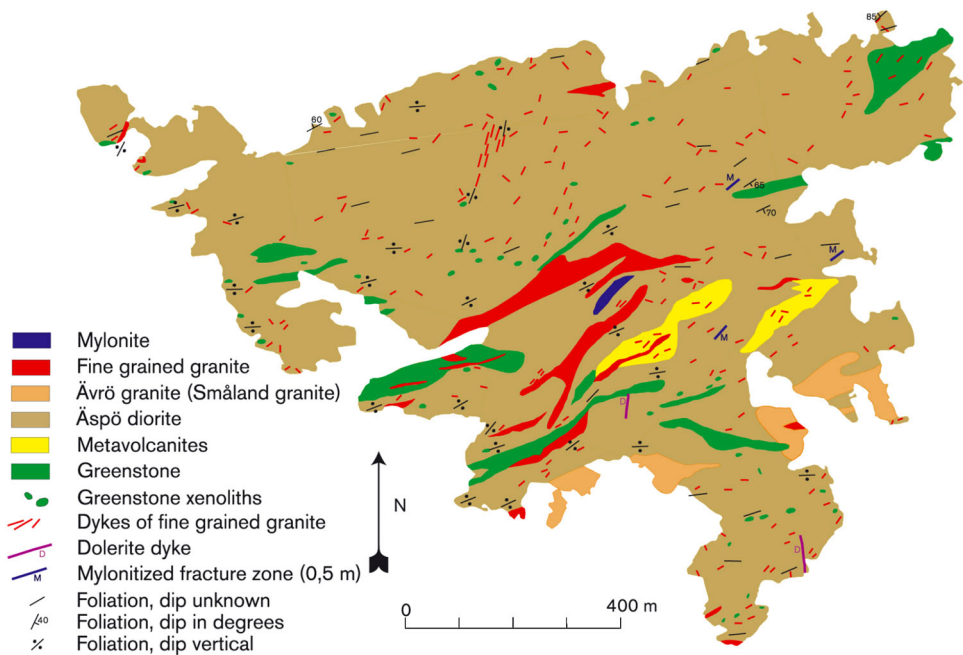


**Fig. 4** Modal composition of Småland granitoids from the Äspö area, showing their large compositional variations (picture reproduced from Berglund et al. 2003)

These are composed of both plagioclase and K-feldspar, of which the reddish K-feldspar megacrysts (10–30 mm) are characteristic for the rock. The samples have suffered from a low-grade metamorphic alteration (cf. Wahlgren et al. 2004) with a strong sericitization and/or saussuritization of plagioclase (> 5 % of plagioclase grains altered). K-feldspar megacrysts generally have a cloudy appearance, are sparsely sericitized and saussuritized and also contain some calcite. No point counting was carried out, but the

composition likely range between quartz monzonite and quartz monzodiorite. The foliation is defined by elongated minerals consisting of partly altered K-feldspar megacrysts, altered plagioclase with sericite and saussurite also striking along the foliation, recrystallized quartz aggregates (subgrains) and biotite, which occur both as single mineral grains as well as aggregates. Accessory minerals are sometimes also parallel to the foliation. Mafic biotite-rich enclaves are abundant in the rock with the strike following the foliation of the rock.

### 3 Methods/Experimental Techniques

#### 3.1 Specimens

Three 241-mm cores from different boreholes, KS0037B02, KS0041B02 and KS0044B02, were used in the experiments. The cores were drilled horizontally out from the TASS tunnel wall (Olsson et al. 2009). Two hourglass-shaped specimens with plane single-curved notches were manufactured from the KS0041B02 and KS0044B02 cores, Fig. 5. The notches were manufactured by careful milling to obtain a smooth surface and to avoid damage on the notch surface. The top and bottom surfaces were ground flat to achieve a good contact to the loading platens. The aim is to obtain a geometry which can mimic the critical area for spalling at a cylindrical borehole or tunnel. The symmetric shape of the specimen (with double notches) is advantageous, since no bending occurs when a concentric load is applied and thus the risk for instability decreases.

The stresses in KS0044B02 were computed using a linear elasticity model with  $E = 66 \text{ GPa}$  and  $\nu = 0.34$ . The notch radii were chosen such that the stress amplification in the notch was about 1.7 times the nominal axial stress in the specimen. The axial stress at the centre of the specimen between the notches was about 1.2 times the nominal stress, see Fig. 6. The notch centre was displaced 50 mm from mid-height along the specimen’s axial direction to obtain a cylindrical area at one of the ends which could be used to determine the nominal stress–strain relation for the cores as in a usual UCS test.

Besides the large specimens, three 50.8-mm cylindrical specimens, drilled out from the third core KS0037B02, were tested to obtain reference data from standard UCS tests.

### 3.2 Specimen Instrumentation

One- and two-directional foil strain gauges (30 and 10 mm gauge length) from Kyowa (2014) were installed on the large specimens. The selection of the 30 mm gauge length was a compromise for the relatively coarse-grained material.

**Fig. 5** Dimensions of the specimens for the spalling experiments

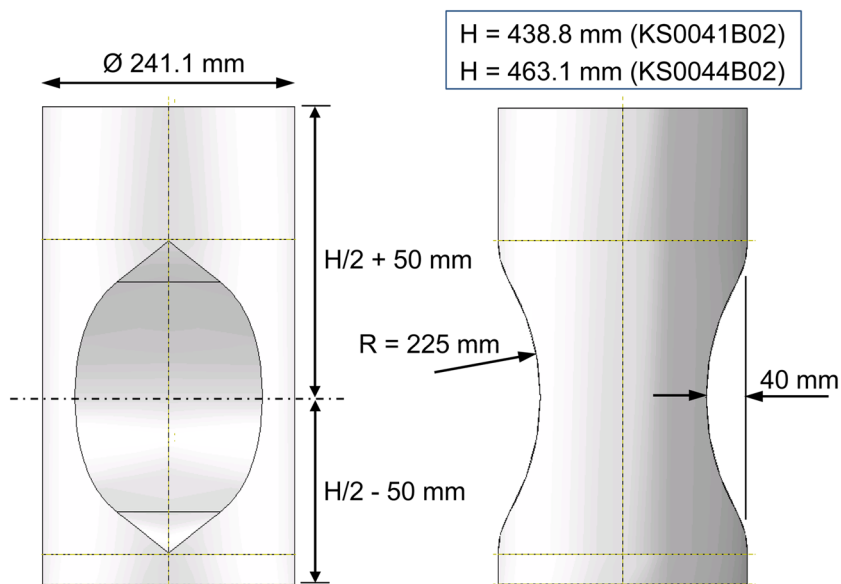


**Fig. 6** Calculated contour plot of the axial stress distribution in specimen KS0044B02 using  $E = 66 \text{ GPa}$  and  $\nu = 0.34$ . The axial displacement of the specimen was set such that the nominal stress becomes 1.00 MPa, yielding 1.70 MPa in the notch and 1.20 MPa in the centre between the notches. This corresponds to an axial force of 45.7 kN

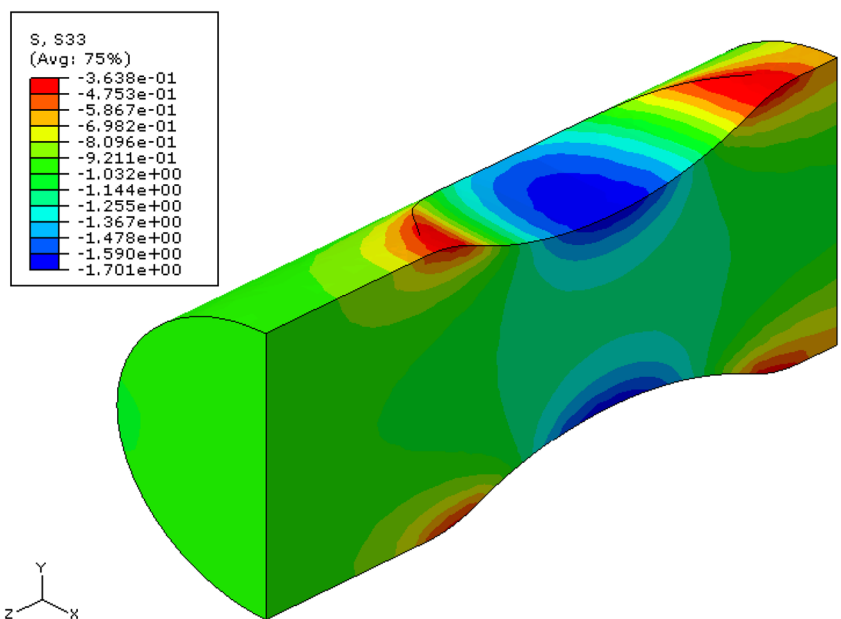


**Fig. 7** Placement of the strain gauges (S) and acoustic emission sensors (AE) for specimen KS0041B02. The total axial deformation measurement is visualized in the *right figure* where the sensors are connected to the upper and lower loading platens. The strain gauges for local measurements and AE sensors have switched sides on specimen KS0044B02

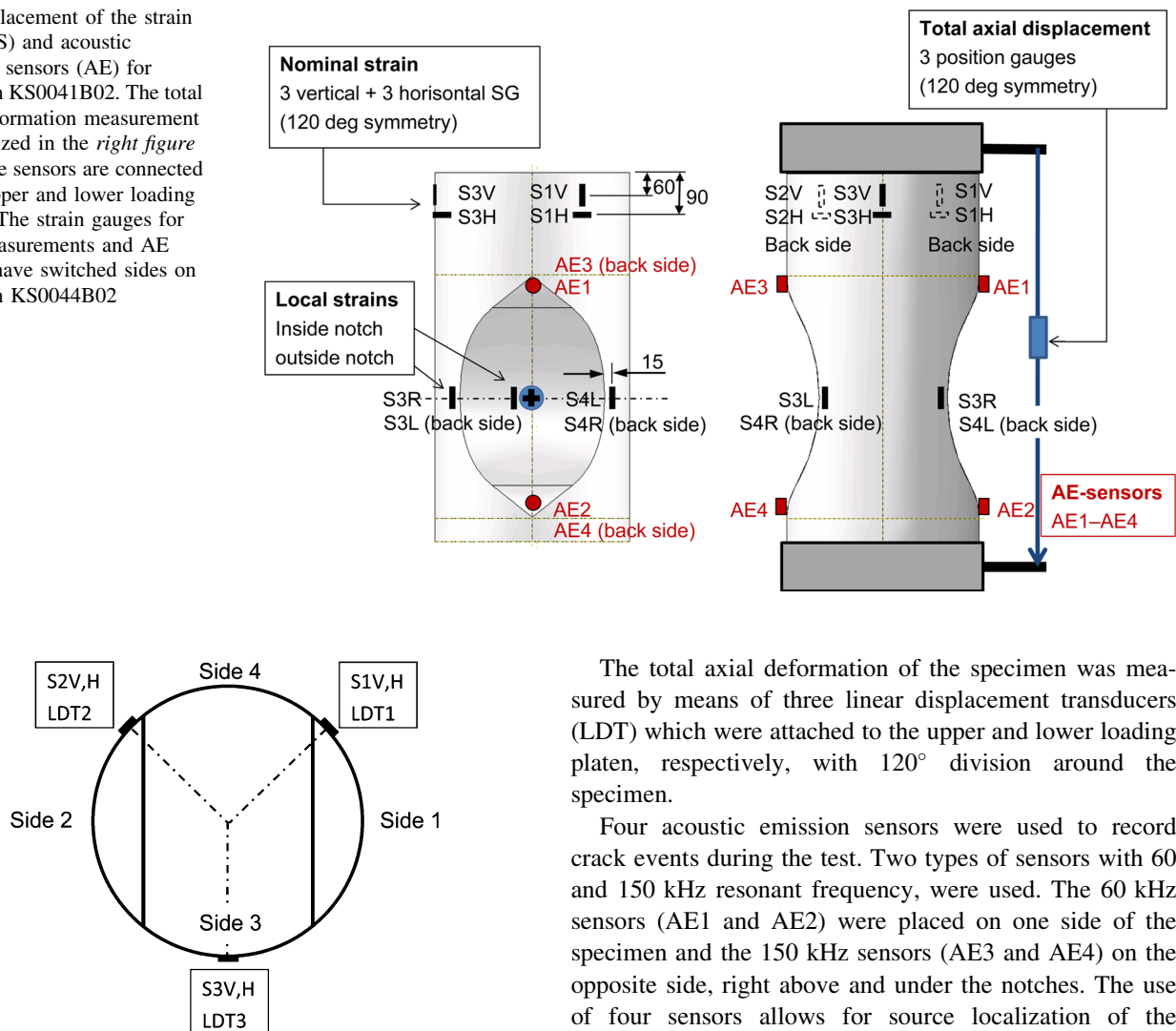


**Fig. 8** Specimen seen from the top with the placement of the strain gauges (S) and total axial deformation measurement (LDT)

The gauge length should be large enough to provide a strain averaging over several grains, but small enough to yield a spatially local value. The 10 mm gauge length was chosen for the two-directional strain gauge as this was the largest available gauge length for this gauge type.

The one-directional strain gauges were placed in both the axial and circumferential directions with 120° division on the cylindrical part of the specimen to monitor the approximately homogeneous uniaxial deformation behaviour. Besides, another set of one-directional strain gauges was placed just outside the notches and yet another was placed exactly in the centre of the notch on one of the notches on each of the two specimens. Finally, a two-directional strain gauge was placed 20 mm to the left of the centrally mounted one-directional strain gauge to measure the axial and transversal strain (Figs. 7, 8).

The total axial deformation of the specimen was measured by means of three linear displacement transducers (LDT) which were attached to the upper and lower loading platen, respectively, with 120° division around the specimen.

Four acoustic emission sensors were used to record crack events during the test. Two types of sensors with 60 and 150 kHz resonant frequency, were used. The 60 kHz sensors (AE1 and AE2) were placed on one side of the specimen and the 150 kHz sensors (AE3 and AE4) on the opposite side, right above and under the notches. The use of four sensors allows for source localization of the recorded acoustic events, either along a line between two sensors or on a plane.

The locations of all sensors are shown in Figs. 7 and 8. The strain gauges were checked using a shunt resistance prior to the tests. The linear displacement transducers were calibrated using gauge blocks and the AE sensors were checked by several pencil lead breaks on the specimen surface. The signals from the load cell, strain gauges and linear displacement gauges were sampled using a HBM MGCplus device (HBM 2014).

### 3.3 Mechanical Loading

A four column load frame with a maximum compressive load of 20 MN was used for the tests, as shown in Fig. 9. The supervision of the tests was made remotely as the test area was sealed off by a wall of concrete blocks in the case of unexpected explosive specimen failure. The specimen was loaded between flat loading platens of hardened steel. A spherical seat was placed over the upper loading platen.



**Fig. 9** Specimen KS0044B02 placed in the load frame right before testing. The concrete blocks sealing off towards the control area are seen in the background

The load was initially measured using a 5 MN electrical load cell. A load of 5 MN would yield a maximum tangential stress of 186 MPa in the notch (according to the FE-simulations) and was estimated to be large enough to produce spalling. The electrical load cell was subsequently removed, as it turned out that fully developed spalling did not take place at a load of 5 MN during the first test (KS0041B02). After that, the load was measured only by means of the hydraulic pressure. The specimens were stored in water until the time for testing to keep high moisture content during the test to reflect the in situ condition.

### 3.4 Macroscopic Analysis

The specimens were cut into half and plane polished slabs, impregnated with fluorescent epoxy, were prepared (Fig. 10). Cracks and fractures were studied and photographed in fluorescence light, and the pictures were adapted in Photoshop Elements to increase the contrasts of the images.

### 3.5 Microscopic Analysis

Thin sections from respective overleaf of the slabs were prepared and impregnated with fluorescent epoxy. The thin sections were photographed via an optical microscopy

aimed for image analysis of microcracks. The thin sections were fixed on a motorized stage programmed so that images were photographed edge by edge, permitting a mosaic of images. The area for each image was  $2.77 \times 2.08$  mm and the image resolution was  $680 \times 512$  pixels. The same area was photographed with fluorescence light and polarized light. These images were later combined in a Zeiss KS400 image processing system creating a combined mosaic of the fluorescent and polarized images. These images were used to determine crack propagation in the specimens.

## 4 Results from Mechanical Experiments

### 4.1 Specimen KS0041B02

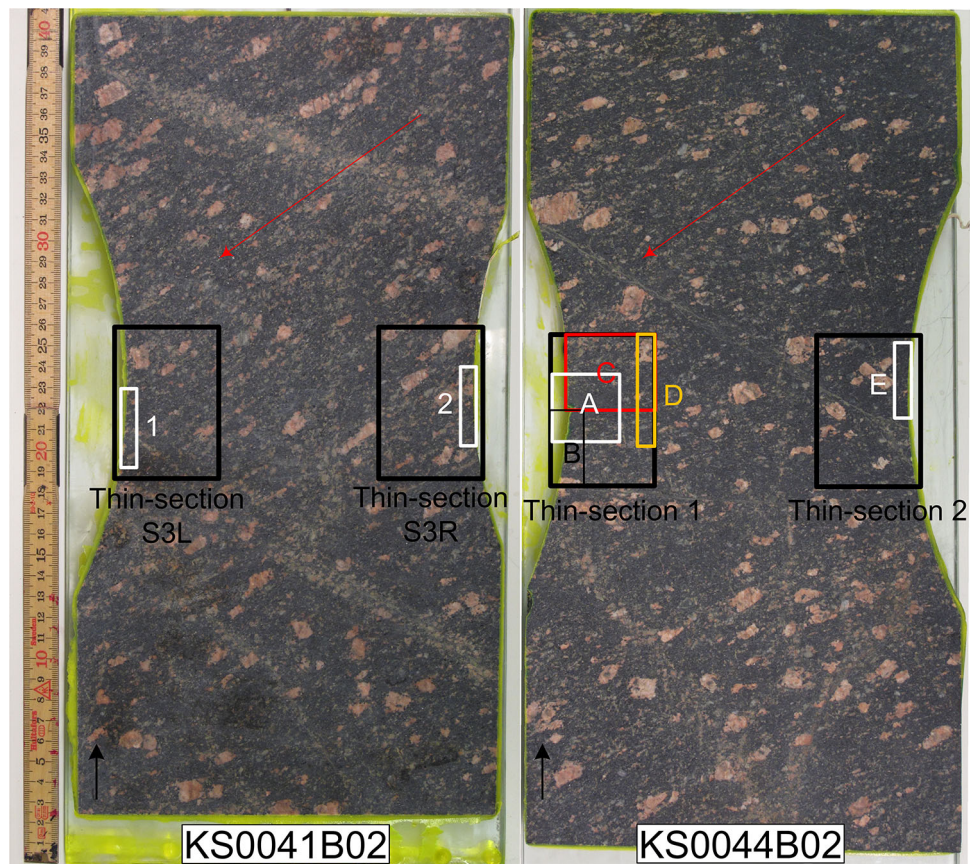
The specimen was first subjected to an axial compression up to 5 MN which was the maximum load for the electrical load cell. One small AE recording was picked up by the sensors at 3.95 MN which was localized between sensor 3 and 4 (side 2), which corresponds to a computed-tangential stress in the notch of 147 MPa. Henceforth, computed-stress values will be shown between parentheses after a load value in the text. The specimen was loaded up to 6.4 MN during the second load cycle after the electrical load cell had been removed. Minor AE signals were recorded before the previous maximum load was reached as expected due to the Kaiser effect. The amplitudes of the AE signals increased with increasing load starting from 5.35 MN (199 MPa). First increase in AE intensity happened around 5.7 MN (212 MPa) which caused a peak in the absolute energy. The first event exceeding 70 dB was exactly between sensor 1 and 2 on side 1 at 5.85 MN (218 MPa). The intensity in the energy accelerated until the test was stopped. Significant recordings were obtained at 6.15 MN (229 MPa).

Results from the strain measurements are shown in Fig. 11. The results are consistent within a few percent difference with values obtained from the FE-model, Fig. 6. A small disturbance was picked up by the strain gauge in the centre of the notch (S1C and S1EC) at 6.21 MN (231 MPa) and the gauge S1C lost the attachment at 6.29 MN (234 MPa).

### 4.2 Specimen KS0044B02

The specimen was loaded up to 5.35 MN and then unloaded. The first AE emission starts between sensor 3 and 4 (side 1) at a load level of 3.00 MN (112 MPa) and a continuous AE activity starts at 3.90 MN (145 MPa). The signal intensifies at 4.5 MN (168 MPa) and severe cracking is registered at 5.15 MN (192 MPa). Results from the

**Fig. 10** Sawn plane polished slabs of specimen KS0041B02 and KS0044B02, impregnated with fluorescent epoxy. The analysed planes are located 50 mm from the centre of the cylinder, see Figs. 5, 6, 7 for dimensions, stress distribution and placement of equipment during mechanical loading. *Large black rectangles* show the position of thin sections, at the centre of the cylinder (different plane than the plane polished slabs). Thin section S3R and thin-section 1 are located at notch at side 1 in Fig. 8, thin-section S3L and thin-section 2 are located at notch at side 2 in Fig. 8. *Smaller rectangles* show the position of microphotographs of the thin sections (Figs. 16, 17, 18, 19, 20, 21). *Black arrows* indicate way up, *red arrows* indicate foliation direction of the specimens



strain measurements are shown in Fig. 12. No deviation was noted in the strain measurements in the notch. Inspection of the specimen shows that cracks have formed and that pieces of rock have spalled out or rather pushed from the surface (Figs. 13, 14, 15). The spalled-off chips are wedge shaped with an angle to the surface plane of 22°–45° which can be seen in Fig. 15. It can be seen that some cracks follow the boundaries of the large mafic enclave (grey/black region in Figs. 13, 14).

#### 4.3 Specimen KS0037B02

Density measurements and uniaxial compression tests (UCS) were carried out on three specimens (KS0037B02-1, -2 and -3) which had a diameter of 50.8 mm and an H/D ratio of 2.51, 2.51 and 2.25. The wet density was determined after storing the specimens for 8 days in water. The mechanical tests were conducted in wet conditions after further 4–7 days storage in water. The axial and circumferential deformations were measured by metal foil strain gauges having a gauge length of 30 mm, three in each direction with a 120° division. Two AE sensors with 60 and 150 kHz resonance frequency, respectively, were attached to the lower loading platen during the test of specimen 2. Loading with AE sensors was only conducted up to severe

cracking was recorded. The sensors were removed before the test was resumed from an unloaded state. Results of the tests are summarized in Table 1 where the volumetric strain method was used (e.g. Nicksiar and Martin 2012) to determine the crack initiation stress  $\sigma_{ci}$  and crack damage stress  $\sigma_{cd}$ . Evaluation of the AE measurement was made according to Diederichs et al. (2004) and yielded a crack initiation stress of 132 MPa. Results from other UCS tests on Äspö diorite are provided in Table 2 for comparison.

#### 4.4 Summary

The results of the AE evaluations from the two spalling tests are summarized in Table 3. The spalling has progressed differently between the two samples and between the two sides on the same specimen. Fully developed spalling with visible fractures could only be seen on side 1 on both KS0041B02 and KS0044B02 specimens. The load was too low to yield fully developed spalling in the other two notches. It is clear that there is a certain variation in the material behaviour when the loads (stress) at the different fracture stages of the four notches are compared.

The elastic properties were evaluated in the large specimens and in the smaller cores and they have similar values:  $E = 66.0$  GPa,  $\nu = 0.35$  (KS0041B02, load cycle



1),  $E = 63.3$  GPa,  $\nu = 0.35$  (KS0044B02) to be compared with the mean values  $E = 65.1$  GPa and  $\nu = 0.34$  of the small cores (KS0037B02). An interesting observation was that the values changed to  $E = 70.1$  GPa and  $\nu = 0.32$  on the second load cycle for specimen KS0041B02 which is an effect of irreversible microcrack closure that occurs at the first load cycle. This effect is also seen on the smaller specimen KS0037B02-2 (Table 1). The elasticity parameters were evaluated as the tangent modulus at an axial stress of 95 MPa for the large specimens and at 50 % of the UCS for the small specimens.

For completeness, it should be mentioned that the procedure regarding moisture handling was somewhat different for the two tests. The specimens were submerged and kept in water for more than one week until the time for testing. This yielded nearly full water saturation. The notch surfaces were wetted several times during the set up and during the test of specimen KS0044B02 whereas this was

not done for specimen KS0041B02. The set up time and test time for load cycle 1 was 4–5 h. The second load cycle was carried out the day after.

### 5 Results from Image Analysis

Mechanical loading caused spalling on side 1 in both specimens, where thin-sections KS0041B02-S3R and KS0044B02-1 later were taken (Fig. 10). Essentially all cracks (including microcracks) developed in the notch area.

#### 5.1 Specimen KS0041B02

In specimen KS0041B02, essentially no microcracks were visible in the combined polarized and fluorescent microscopic images of thin-section S3L, side 2 (Fig. 16). However, in the fluorescent images of both thin sections of the

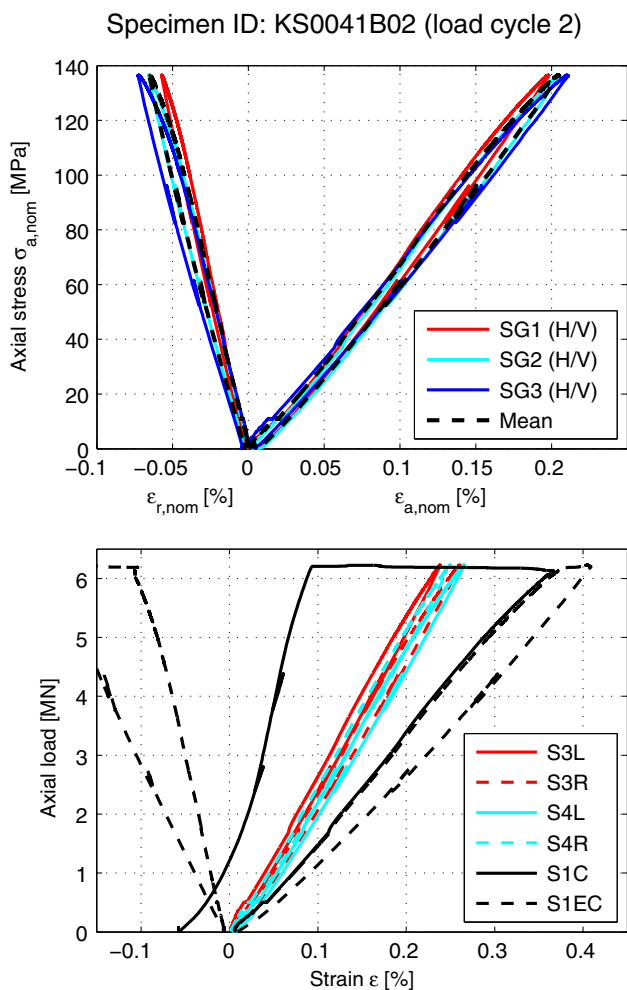


**Fig. 11** Results from KS0041B02 (load cycle 2). *Upper figure* nominal axial stress vs. strain; *lower figure* axial load vs. local strains just outside the notch (S3 and S4) and in the centre of the notch (S1)

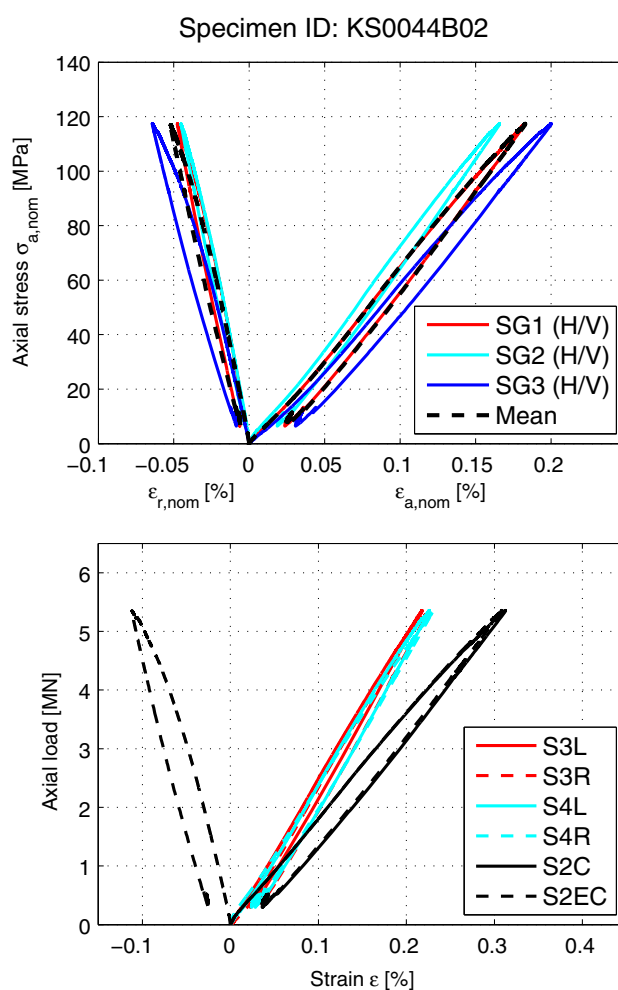


**Fig. 12** Results from KS0044B02 (load cycle 2). *Upper figure* nominal axial stress vs. strain; *lower figure* axial load vs. local strains just outside the notch (S3 and S4) and in the centre of the notch (S2)



**Fig. 13** Front view of the spalling area at side 1 on KS0044B02. Chips have fallen off in the darker areas (cf. small photo of the same area before testing). The holes after the missing rock are like small craters. The extent of the fractures is marked with red lines (about 75 mm × 45 mm)

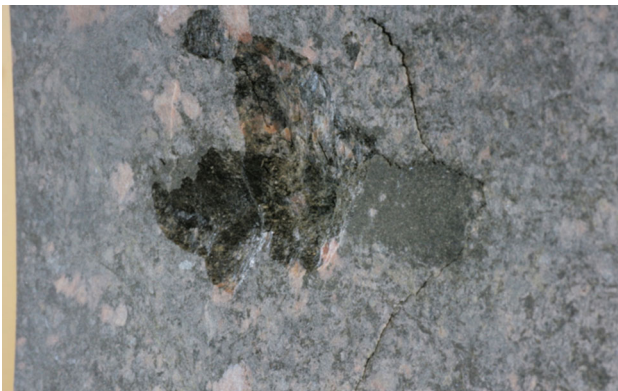


**Fig. 14** Close-up of the spalling area at side 1 on KS0044B02 seen from the right to get a depth perspective of the spalling area. Material is missing in the darker areas. The holes after the missing rock are like small craters

specimen, thin microcracks were visible around several quartz grains (cf. Fig. 16). Biotite was occasionally also surrounded by thin, hardly visible microcracks. Feldspars generally lacked grain boundary cracks, but sometimes held intragranular cracks mainly along cleavage planes. In thin-section S3L very thin, up to 10 mm-long-intragranular cracks sub-parallel to the direction of  $\sigma_1$  occurred up to 40 mm from the notch within the feldspar megacrysts. By the notation  $\sigma_1$  we mean the largest macroscopic compressive principal stress. It should be noted that the local stress field at a grain scale can vary. Intragranular cracks also occurred within biotite, but along its basal cleavage plane rather than along  $\sigma_1$ .

In thin-section S3R (side 1) one major, slightly undulating fracture developed parallel to the surface, 4 mm



**Fig. 15** Chips that have fallen off specimen KS0044B02 from side 1. The pieces are up to 25–28 mm long, thickness/depth about 5 mm

**Table 1** Results from the tests on 50.8 mm cores

Specimen ID	$\rho$ (kg/m <sup>3</sup> )	$E$ (MPa)	$\nu$ (–)	$\sigma_{ci}$ (MPa)	$\sigma_{cd}$ (MPa)	UCS (MPa)
KS0037B02-1	2,770	65.6	0.33	98.2	161.4	187.5
KS0037B02-2a <sup>b</sup>	2,780	66.8 <sup>a</sup>	0.37 <sup>a</sup>	109.1	165.7	–
KS0037B02-2b <sup>b</sup>	–	69.1	0.36	–	–	214.2
KS0037B02-3	2,780	62.9	0.32	107.6	164.3	206.8
Mean values	2,777	65.1	0.34	104.9	163.8	202.8

<sup>a</sup> Evaluated using a UCS value of 214.2 MPa

<sup>b</sup> 2a is first loading, 2b is second loading

**Table 2** Results on Äspö diorite from Staub et al. (2004)

Borehole	$\rho$ (kg/m <sup>3</sup> )	$E$ (MPa)	$\nu$ (–)	$\sigma_{ci}$ (MPa)	$\sigma_{cd}$ (MPa)	UCS (MPa)
KA3376B01 <sup>a</sup>	2,730	68	0.28	87.1	179	199
KQ (strain) <sup>b</sup>	2,755	76	0.27	96.3	199	216
KQ (AE) <sup>b</sup>	2,755	76	0.27	121	204	216

<sup>a</sup> Mean value of two specimens and using the strain method

<sup>b</sup> Mean value of five specimens from boreholes KQ0064G01, KQ0064G07 and KQ0065G01

from the perimeter of the notch, and parallel to the major principal stress field ( $\sigma_1$ ), see Fig. 17a. Whereas the main direction was controlled by the major principal stress field ( $\sigma_1$ ), the  $\sigma_1$ -parallel cracks generally cut straight through quartz and feldspars independent of the crystal structure. The undulation was caused by cracks deviating from this trend, going around quartz- and feldspar grains (as grain boundary cracks) or along planes in the crystal lattice in

**Table 3** Different stress thresholds for the fracture stages for the two large specimens

Specimen	Stage	Load (MN)	Stress (MPa)	Sensor	Side	Comment
KS0041B02	First act	3.95	147	3–4	2	Spalling chips on side 1
KS0041B02	Initiation	5.35	199	–	–	Specimen surface dried for 4 hours
KS0041B02	Coalescence	5.85	218	1–2	1	
KS0041B02	Damage	6.15	229	1–2	1	
KS0044B02	First act	3.00	112	3–4	1	Spalling chips on side 1
KS0044B02	Initiation	3.90	145	3–4	1	Surface kept wet during the test
KS0044B02	Coalescence	4.50	168	3–4	1	
KS0044B02	Damage	5.15	192	3–4	1	

feldspar (as intragranular grains). When the cracks reached biotite they rarely crossed the mineral grains, but almost exclusively followed the grain boundaries around the mineral grains or the planes in the crystal lattice within the biotite, causing a zigzag-like pattern. Around the main fracture, several microcracks developed oriented sub-parallel to  $\sigma_1$ , but with a slight inclination towards the surface. These cracks were generally parallel to crystal cleavage plane {010} in the plagioclase. Hence, it was probably the crystal cleavage planes that governed the crack propagation direction. The main crack kinked back several times along its extension to become parallel to the  $\sigma_1$  direction. The main part of the cracks were located within or crosscutting larger feldspar megacrysts. The cracks were also wider in the feldspars and tended to get thinner around the micas. The area at the missing chip in the upper part of Fig. 17a was surrounded by cracks parallel to the cleavage planes in the crystal lattice of the feldspar grain above marked area B in Fig. 17a as well as grain boundary cracks along micas which were parallel to the foliation of the specimen. Within the inner part of the thin-section feldspar hosted thin, hardly detectable, 2.5–5 mm-long-intragranular cracks and sparsely also microcracks crossing the feldspar boundaries, of which the longest is 15 mm (10 mm from the notch). These cracks occur up to 40 mm from the notch in thin-section S3R.

## 5.2 Specimen KS0044B02

The cracks in specimen KS0044B02 were more disturbed than in specimen KS0041B02. Fracturing and spalling were generated where thin-section 1 (side 1) was located and a large chip was missing in the thin section (Figs. 10, 18, 19, 20). As seen in Fig. 17, fractures were relatively heterogeneous, but the main orientation was parallel to loading and  $\sigma_1$ , in connection to the perimeter of the notch. Microcracks also developed mainly parallel to  $\sigma_1$  (Figs. 19, 20, 21).

The cracks in specimen KS0044B02 were more disturbed than in specimen KS0041B02. As seen in Figs. 18

and 20, several larger fractures were developed with a conical appearance with the base of the cone facing the perimeter of the notch, in contrast to specimen KS0041B02, where the main fracture basically was parallel to  $\sigma_1$ . Fracturing and spalling were generated where thin-section 1 (side 1) was located and a large chip was missing, as seen in the plane polished slab and thin section (Figs. 18, 19, 20). The cracks were relatively heterogeneous, with the main orientation of the fracture parallel to loading and  $\sigma_1$  (in connection to the perimeter of the notch), although cracks also developed along the foliation of the rock and especially along the foliation of a mafic enclave, which was striking along its foliation. Single intragranular microcracks within the interior of the specimen were developed mainly parallel to  $\sigma_1$  (Figs. 19, 20, 21)

Within the mafic enclave (darker area striking from the notch along the main foliation of the rock), two main cracks were developed. One of these cracks crosscut the foliation of the mafic enclave, approximately following  $\sigma_1$ , whereas the other crack was oriented roughly along the foliation of the mafic enclave. The cracks within the mafic enclave preferentially propagated towards the border of the enclave. The crack propagating inwards, along its foliation, generally propagated along grain boundaries of biotite within the enclave. The crack was subdivided near the boundary of the mafic enclave. One crack plunged upwards about 20 mm from the notch, through feldspars parallel to  $\sigma_1$ , whereas several smaller cracks were spreading and thinning inwards, towards the edge of the enclave, with one of these following the boundary before finally being thinned out and disappeared. Smaller foliation-oriented microcracks were sparsely distributed within the mafic enclave (Fig. 20).

The microcrack plunging away from the mafic enclave (Fig. 20), stroke roughly parallel to  $\sigma_1$  and displayed a similar pattern as cracks developed near the notch in Fig. 19. These cracks generally cut straight through quartz and feldspars, whereas they followed the grain boundaries of biotite. The main part of the microcracks was located within or crosscut larger K-feldspar megacrysts (cf.

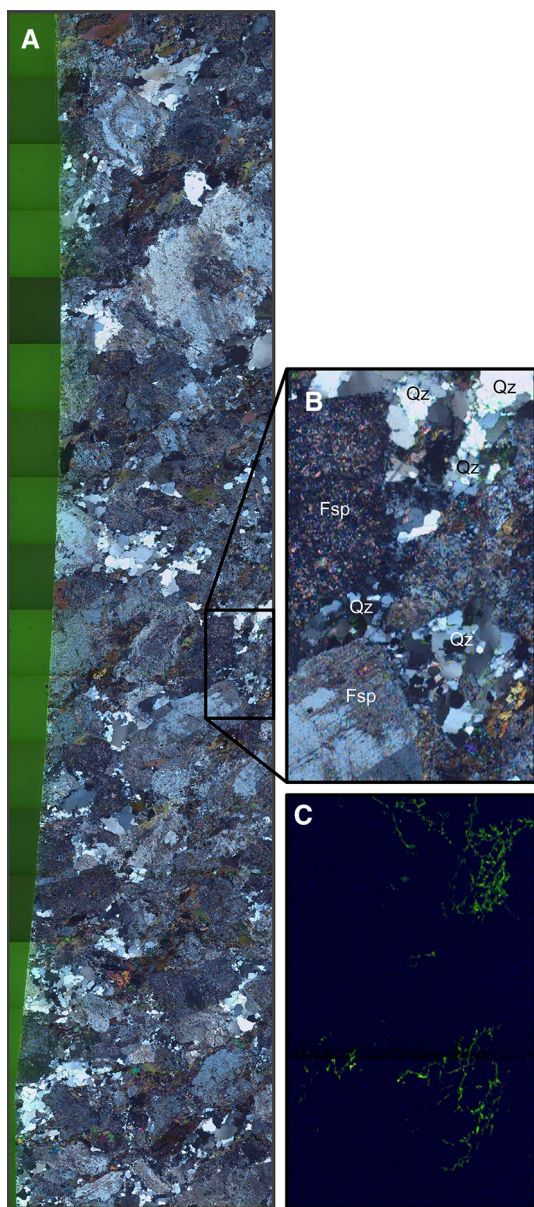


**Fig. 16** **a** Combined polarized and fluorescent microscopic image of KS0041B02 thin-section S3L Image 1 (see Fig. 10). Image size is  $8.3 \times 37.4$  mm. **b** Close-up of **a**. *Fsp* feldspar, *Qz* quartz. **c** Fluorescent microscopic image, same view as **b**

Fig. 19). Intragranular microcracks occurred up to 40 mm from the notch and were located within the feldspar megacrysts, the cracks oriented roughly parallel to  $\sigma_1$  (Figs. 20, 21). The largest of these cracks seemed to be located in an area/field roughly striking  $30^\circ$  to the left, sub-parallel to the notch.

The microcracks in thin-section 2 (side 2) were preferentially located parallel to  $\sigma_1$  within feldspar megacrysts (Fig. 22, red arrows pointing at microcracks), whereas grain boundary cracks essentially were absent. Longer microcracks (up to 10 mm) were exclusively located within the feldspar megacrysts. Some microcracks were

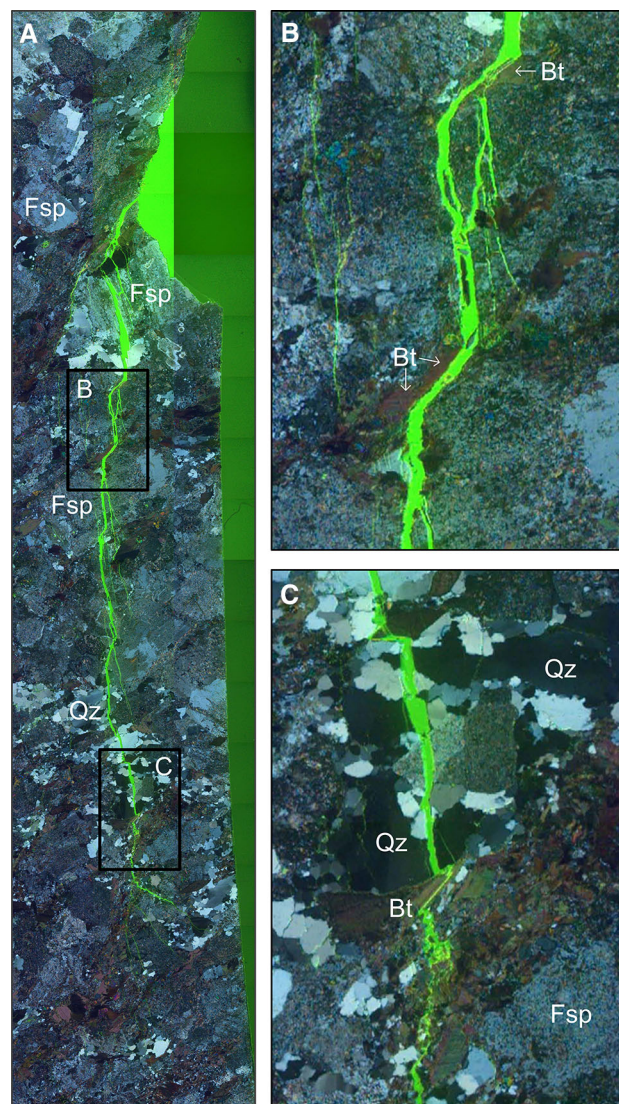


**Fig. 17** **a** Combined polarized and fluorescent microscopic image of specimen KS0041B02 thin-section S3R Image 2 (see Fig. 10). Image size of **a** is  $8.3 \times 37.4$  mm. **b**, **c** are close-up images of **a**. *Bt* biotite, *Fsp* feldspar, *Qz* quartz

also oriented perpendicular to  $\sigma_1$ , within the feldspar megacrysts. Microcracks were sparsely spread all over the thin section, but were more common closer to the notch.

## 6 Discussion

### 6.1 Test Setup

The design with a symmetric specimen yields a possibility to acquire data from both notches independent of each other, since it can be assumed that there is a negligible interaction of the fracturing processes between the notches. To separately follow the fracture processes of the two

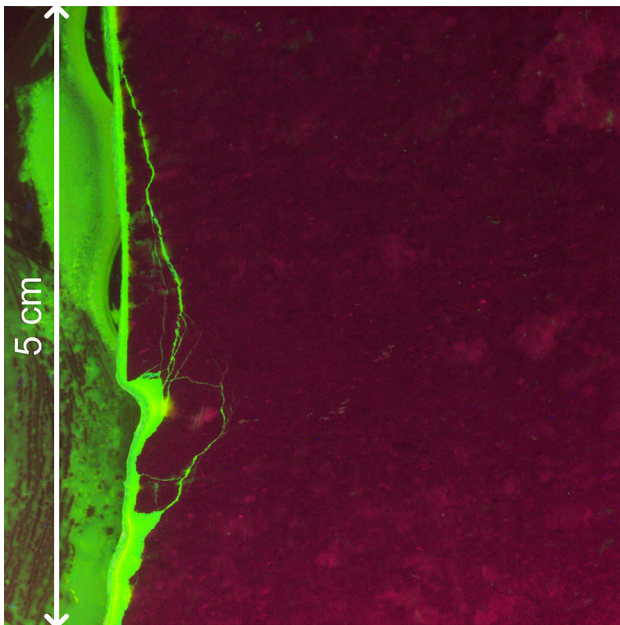


**Fig. 18** Plane polished slab of specimen KS0044B02 Image A (see Fig. 10), impregnated with fluorescent epoxy. The contrast and intensity of the image has been increased in Photoshop Elements

notches, it requires that a source location of the AE events can be made, since the AE measurements were used for the crack monitoring. It was seen that the mechanical loading caused fracturing and spalling in the four notches at different stress levels. This displays the natural variation within the rock material.

As to the AE measurements, the 150 kHz sensors appeared to pick up acoustic signals better than the 60 kHz sensors. This made the evaluation of the acoustic events difficult and may have caused a bias when data at the two notches were evaluated on the specimens. Despite this, it was possible to obtain source located data to a certain extent. With this we could identify the different fracture stages and at which notch the actual fracture stage first occurred, which was the main aim of the AE monitoring.

It can be recommended for further studies to use AE sensors with a suitable resonance frequency, in this study 150 kHz, to obtain good fracture event monitoring. An alternative is to use sensors with broadband spectrum. This alternative was not examined by the authors.

The strain measurements gave no response of spalling initiation, but gave only indications of fracturing at a very late stage on specimen KS0041B02. This result should be kept in mind for other similar tests if strain gauges will be the main measurement and indicator of spalling.

## 6.2 Microcrack Observations

Essentially all cracks are related to the main fracture in the notches, although some microcracks were generated near

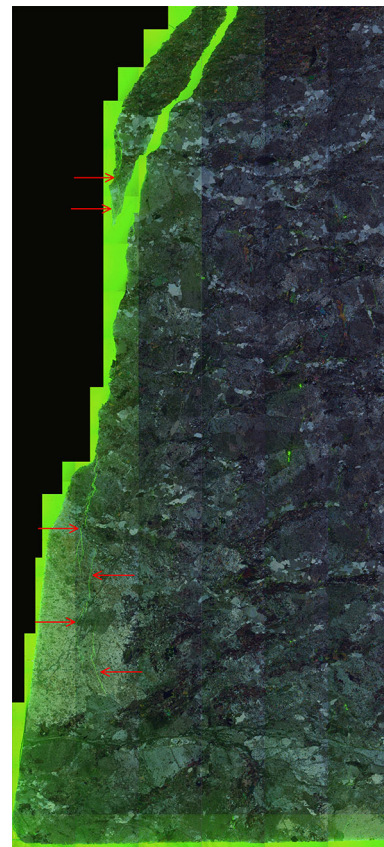


**Fig. 19** Combined polarized and fluorescent microscopic image of specimen KS0044B02 thin-section 1 Image B (see Fig. 10). Image size is 16.6 × 36.8 mm. Arrows indicate microcracks

one of the notches that did not develop spalling (Fig. 22). Fracturing may thus be initiated as these  $\sigma_1$ -sub-parallel microcracks located within feldspar megacrysts. The majority of the fractures seem to be caused by extension along the major principal stress field ( $\sigma_1$ ), although some shearing occurred as indicated by small displacements along the main fracture path (see Fig. 23). Since the epoxy impregnation of the specimens was carried out at an unloaded state, the shear deformations must have been larger at a loaded state.

Microcracks are classified as intragranular- (within a mineral grain), transgranular- (crossing more than one grain) and grain boundary cracks (Kranz 1983). However, we do not distinguish between the intra- and intergranular cracks here. It is also important to distinguish contacts between grains of the same mineral type, such as quartz–quartz mineral contacts and phase contacts between different type of minerals e.g. quartz–feldspar grains. The latter are two different phases with different strengths, stiffness and surface energies. This leads to higher stress concentrations in the phase contact and, hence, influences the mechanical properties of the rock such as crack initiation stress (Åkesson et al. 2001; Lindqvist et al. 2007).

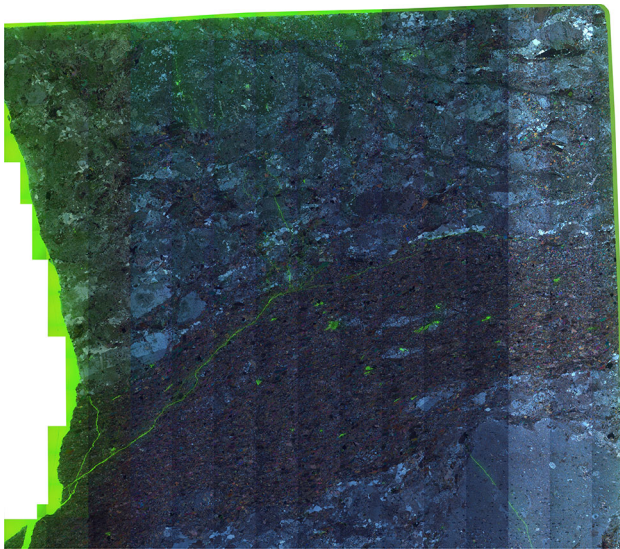


**Fig. 20** Combined polarized and fluorescent microscopic image of specimen KS0044B02 thin-section 1 Image C (see Fig. 10). Image size is  $41.6 \times 35.6$  mm. Crack in the large K-feldspar megacryst, by the corner on the right-hand side, follows the joint in polarized image (somewhat darker line), although the fluorescent image showing the green crack is missing

Also the grain size matters as the general trend points towards higher strength in finer grained rocks of the same rock type. Larger mineral grains (or phase aggregate grains for that matter) also act as greater critical disorders. In contrast, fine-grained sericite in altered feldspar may increase the fracture toughness (Lindqvist et al. 2007). These fine mica grains grow across the major cleavage plane and act as energy barriers for propagating cracks.

Grain boundary cracks within the matrix of the granitoids are more common in specimen KS0041B02 (Fig. 16), which merely reflects the abundance of quartz grains/aggregates. In contrast, specimen KS0044B02 lacks larger quartz aggregates. In general grain boundary cracks are not as common as intragranular and transgranular grains and the grain boundary cracks are rarely coupled to transgranular cracks, fracturing and spalling. This is in accordance with results on granite subjected to compression (Kranz 1983).

Spalling cracks in quartz grains are almost solely transgranular and oriented parallel to  $\sigma_1$ , cutting straight through the mineral grains, regardless of the crystal lattice direction. Hence, the direction of the stress field controls the direction of the spalling cracks in quartz.

Feldspars response to fracturing is more complex. The majority of the microcracks are intragranular or transgranular and oriented parallel to  $\sigma_1$  (Figs. 19, 20, 21). However, the direction of  $\sigma_1$  roughly coincides with cleavage planes in the crystal lattice of the feldspars. Hence

**Fig. 21** Combined polarized and fluorescent microscopic image of specimen KS0044B02 thin-section 1 Image D (see Fig. 10). Image size is  $7.7 \times 54.3$  mm



it is impossible to say whether the cracks preferentially propagate through the crystal lattice or if they merely follow  $\sigma_1$ .

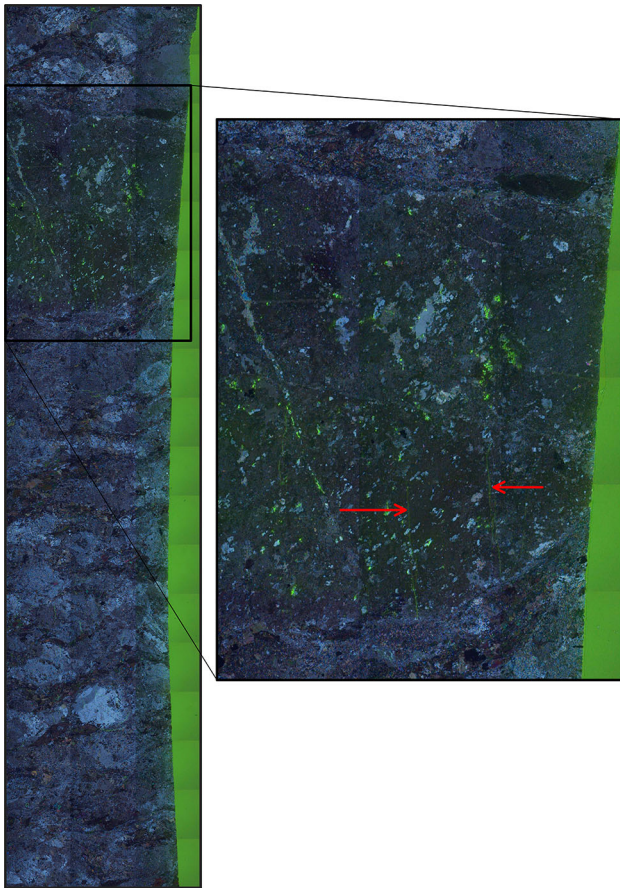


**Fig. 22** Combined polarized and fluorescent microscopic image of specimen KS0044B02 thin-section 2 Image E (see Fig. 10). Image size is  $8.3 \times 37.4$  mm. Arrows show intragranular cracks within altered feldspar

For biotite, propagating cracks deflects and sweep along the grain boundaries (as transgranular cracks) or along its basal crystal cleavage plane  $\{001\}$  rather than across other cleavage planes as much more energy is needed to cross the cleavage planes in directions deviating from the  $\{001\}$  direction (e.g. Kronenberg et al. 1990). The orientation of biotite grains significantly govern the crack propagation either by providing favourable fracture growth paths or by terminating the cracks where biotite grains were oriented perpendicular to the main fracture path. As for biotite, in which the properties of the material control the behaviour of the crack propagation rather than the stress field, the major crack in the mafic enclave (Fig. 20) preferentially propagates along its foliation, sweeping along the grain boundaries of biotite (Åkesson et al. 2003). Hence, it seems the  $\sigma_1$  stress field along with the biotite foliation control the direction of the crack propagation within the mafic enclave. For fractures propagating in a high angle to the foliation this results in a zigzag pattern due to the

interaction with micas oriented with an high angle to the fracture and thus acting as energy barriers and weak grain boundaries and basal cleavage plane in the micas (Fig. 20).

It was previously observed that the main fracture as seen in thin section S3R (Figs. 17, 23) follows the  $\sigma_1$  direction even though several minor fractures with a small inclination towards the surface starting from the main crack path suddenly ends. If loading was continued or if relaxation was caused by e.g. spalling on the outside, then extension within the rock would presumably allow propagation along  $\sigma_1$  of these cracks (Fig. 23). However, as it is now, these cracks generally ends when reaching biotite grains, which act as an energy barrier for the crack propagation. Hence, the fracture path is influenced by the favourably oriented pre-existing microstructural fabric of the rock. In many cases the orientation of biotite grains is dictating the local direction for fracture growth, which is an observation that is in agreement with Nasserri et al. (2011) and Mahabadi (2012).

Most cracks developed in connection with the open-spalling fractures propagate from them as transgranular cracks. However, large intragranular cracks are also found parallel to  $\sigma_1$  in the interior of the thin sections, within K-feldspar megacrysts, suggesting that crack initiation probably started in these grains. Intragranular cracks are usually larger in “unaltered” feldspar megacrysts, where they propagate more easily. The lack of large “unaltered” K-feldspar megacrysts by the notches that did not develop spalling may also explain why spalling was favoured on one side of each specimen. Specimen KS0044B02, with the more complex crack propagation further includes a mafic enclave. Hence, these heterogeneities probably act as critical disorders for the crack initiation.

Double-wedged chips such as the one lacking in Fig. 17a, have probably formed prior to the fractures described above. The wedge angles are in the range of  $22^\circ$ – $45^\circ$  which points on that a shear mechanism and subsequent dilation are responsible for the fracturing. In specimen KS0044B02, several larger fractures were developed with this conical appearance (with an angle of approximately  $20^\circ$ – $60^\circ$ ) with the base of the cone facing the perimeter of the notch. This is in contrast to specimen KS0041B02, where the main fracture basically is parallel to  $\sigma_1$ . Towards the end of the main fracture in specimen KS0041B02, however, the fracture offsets in the range of  $20^\circ$ – $60^\circ$  (Figs. 17, 23). Hence, crack propagation probably follows  $\sigma_1$  along with the foliation of the rock, but before spalling can take place the fractures offset towards the perimeter of the notch, with an angle between  $20^\circ$  and  $60^\circ$ , sometimes causing conical spalling chips. As seen in Fig. 17a, the area at the missing chip is surrounded by cracks parallel to the cleavage planes in the crystal lattice

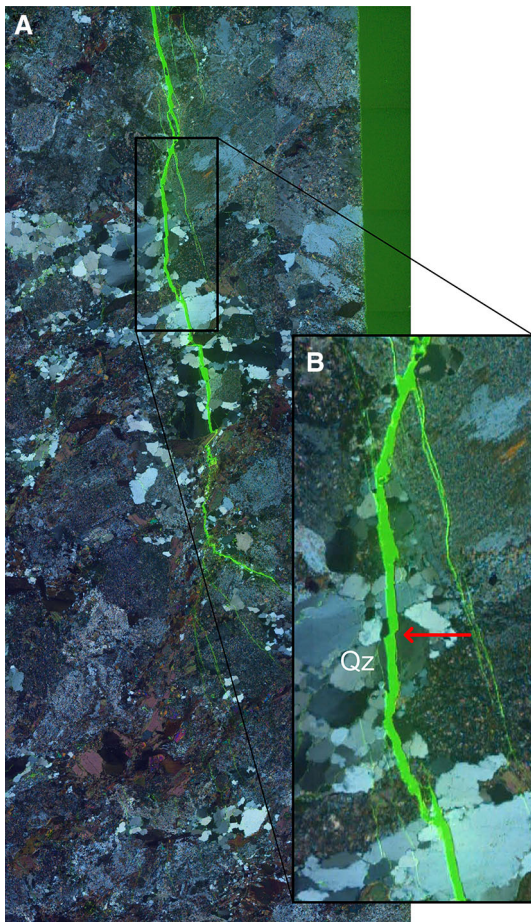


**Fig. 23** Combined polarized and fluorescent microscopic image of specimen KS0041B02, where **a** is the lower half of Fig. 17 (image size of **a** is  $8.3 \times 18.7$  mm). *Arrow* points at a location where a shear displacement can be seen

of the feldspar grain above marked area B in Fig. 17a as well as grain boundary cracks along micas within a minor mafic enclave, parallel to the foliation of the rock. The other explanation is thus that cracks parallel to  $\sigma_1$  offset along cleavage planes in the crystal lattice of feldspars as well as along grain boundaries of e.g. micas or mafic enclaves. When these propagating cracks/fractures meet, chips may fall out of the notch.

### 6.3 Effect of Stress Gradient

It was seen in Fig. 17 that in specimen KS0041B02 a main fracture was formed in the notch about 4 mm from the surface. Except for a few fractures near the vicinity of the main fracture the material is almost free from cracks in the area towards the free surface. Figures 19 and 22 show fractures 2 mm and more from the notch parallel to  $\sigma_1$ . This may be compared with the results from compression of blocks with borehole diameter of 22 mm on an equigranular fine- to-medium-grained granite (Westerly

granite) by Haimson (2007). Figures 4–7 in Haimson (2007) show that many fractures were developed parallel to the surface starting from a distance of less than 0.25 mm from the surface. Another observation is that the fracture in the current experiment kinks a few times when barriers, in this case biotite grains, are met. The fracture is partly guided by the microstructure. The fractures shown in Haimson (2007) seem to be almost straight and cut through the grains. These differences could be an effect attributed to the different hole radii and thus different stress gradients in the vicinity to the hole surface.

### 6.4 Crack Initiation Stress and Mineral Strengths

What are the common mechanisms that make a UCS test useful for obtaining data for crack initiation in underground openings? Hallbauer et al. (1973) found that failure of embedded point-loaded quartzite grains was a frequent source of microcrack initiation in quartzite. It was found by Eberhardt et al. (1999a) that the feldspar and quartz mineralogy was responsible for the crack initiation and secondary cracking respectively in grey granite. Similar behaviour could be seen in a coarser grained pegmatite, but at slightly lower stress levels. These results along with the observations made in current tests, it is concluded that fracture development in feldspar was responsible for the crack initiation threshold. Minor differences would be observed if these grains were embedded in a cylindrical specimen, in the type of specimen described in the current study or even in a rock mass. The weakest embedded grains will fail first and consequently AE observations will to some extent be comparable between different tests on the same material. However, the propagation may be different due to e.g. actual stress gradient or feedback confinement. The in situ case requires more complicated reasoning about the initiation since the surfaces are rough and may have a higher amount of existing microcracks from excavation or drilling operations and thus may trigger other fracture initiation phenomena. The studied Äspö diorite displays weak links in feldspar in general and particularly in K-feldspar megacrysts.

## 7 Conclusions

This paper presents results from a new type of tests where spalling initiation and crack formation can be studied in detail. The choice of radius of the notch creates a stress gradient similar to that at a large circular opening, such as e.g. a deposition hole within a nuclear waste repository. The results should be applicable to other cases with a large hole diameter such as tunnel circuits. It was possible to determine thresholds of crack initiation and secondary



cracking by monitoring fracture events using AE. Moreover, wedge-shaped rock chips were formed and fell off the surface at an early stage of spalling. These chips can be compared with the early fracturing seen at the in situ test on Äspö diorite (APSE) which looks more like a fish scale pattern with thin flakes.

The development of fractures in the specimens was studied in depth at the grain scale on polished slabs and also in thin sections. The spalling fractures essentially developed parallel to loading, close to the perimeter of the notches and is caused by extension along the major principal stress field ( $\sigma_1$ ). Some shearing must also have occurred as indicated by small displacements along the main excavation. Spalling cracks are transgranular, slightly undulating, cutting straight through most mineral grains, although they sweep along and may be deflected by biotite grain boundaries. Intragranular microcracks within K-feldspar megacrysts occur sparsely throughout the thin sections. The results indicate that crystallographic cleavage planes in the larger feldspar grains and mafic enclaves act as critical disorders for the crack initiation.

The weakest constituents in the rock material fail first, e.g. quartz-, feldspar grains or mafic enclaves, which defines a lower limit of the crack initiation. These failed grains together with other flaws such as pre-existing microcracks and pores are critical locations for crack propagation. The main cracks, 2–4 mm below the notch surface, propagate mainly parallel to the direction of the macroscopic  $\sigma_1$  field, but deflect at many locations away from the direction of  $\sigma_1$ , due to orientations of the minerals along the path. However, they kink back again to align with the stress field. Hence, the main crack path is controlled by both the macroscopic stress field and the local microstructure.

The existence of biotite grains in the rock material is an important factor for the crack propagation paths. Biotite grains can act as a crack terminator, but they may also deflect the crack path depending on the crystallographic orientation of the actual grains. Some fracturing indicates that a shear component is present and not only a tensile fracturing process. Further experimental investigations can hopefully clarify this issue.

In summary, this type of test design provides increased understanding of crack initiation and crack formation in crystalline rock. The results on stress levels associated with different fracture stages and how cracks propagate provide useful input for creating and verifying realistic computer models of rock fracturing processes at the grain scale, e.g. synthetic rock mass models.

**Acknowledgments** The work was supported by the Swedish Nuclear Fuel and Waste Management Co.

## References

- Åkesson U, Lindqvist JE, Göransson M, Stigh J (2001) Relationship between texture and mechanical properties of granites, central Sweden, by use of image-analysing techniques. *Bull Eng Geol Environ* 60(4):277–284. doi:10.1007/s100640100105
- Åkesson U, Stigh J, Lindqvist JE, Göransson M (2003) The influence of foliation on the fragility of granitic rocks, image analysis and quantitative microscopy. *Eng Geol* 68(3–4):275–288. doi:10.1016/S0013-7952(02)00233-8
- Andersson JC (2007) Rock mass response to coupled mechanical thermal loading: Äspö pillar stability experiment. PhD thesis, Royal Technical University, Stockholm
- Autio J (1997) Characterization of the excavation disturbance caused by boring of the experimental full scale deposition holes in the research tunnel at olkiluoto. SKB TR-97-24, Swedish Nuclear Fuel and Waste Management Co., Stockholm
- Berglund J, Curtis P, Eliasson T, Olsson T, Starzec P, Tullborg EL (2003) Äspö Hard Rock Laboratory-Update of the geological model (2002) International Progress Report IPR-03-34. Swedish Nuclear Waste Management Co., Stockholm
- Brace WF, Paulding BW, Scholz C (1966) Dilatancy in the fracture of crystalline rocks. *J Geophys Res* 71(16):3939–3953. doi:10.1029/JZ071i016p03939
- Carter BJ (1992) Size and stress gradient effects on fracture around cavities. *Rock Mech Rock Eng* 25(3):167–186. doi:10.1007/BF01019710
- Carter BJ, Lajtai EZ, Petukhov A (1991) Primary and remote fracture around underground cavities. *Int J Num Anal Meth Geomech* 15(1):21–40. doi:10.1002/nag.1610150103
- Cho N, Martin CD, Segoo DC, Jeon J (2010) Dilation and spalling in axially compressed beams subjected to bending. *Rock Mech Rock Eng* 43(2):123–133. doi:10.1007/s00603-009-0049-x
- Daemen JJK, Fairhurst C (1971) Influence of failed rock properties on tunnel stability. In: Clark GB (ed) Proceedings of 12th U.S. symposium on rock mechanics. University of Missouri-Rolla, AIME, New York, pp 855–875
- Diederichs MS, Kaiser PK, Eberhardt E (2004) Damage initiation and propagation in hard rock during tunnelling and the influence of near-face stress rotation. *Int J Rock Mech Min Sci* 41(5):785–812. doi:10.1016/j.ijrmms.2004.02.003
- Eberhardt E (2001) Numerical modelling of three-dimension stress rotation ahead of an advancing tunnel face. *Int J Rock Mech Min Sci* 38(4):499–518. doi:10.1016/S1365-1609(01)00017-X
- Eberhardt E, Stead D, Stimpson B, Read RS (1998) Identifying crack initiation and propagation thresholds in brittle rock. *Can Geotech J* 35(2):222–233. doi:10.1139/t97-091
- Eberhardt E, Stimpson B, Stead D (1999a) Effects of grain size on the initiation and propagation thresholds of stress-induced brittle fractures. *Rock Mech Rock Eng* 32(2):81–99. doi:10.1007/s006030050026
- Eberhardt E, Stimpson B, Stead D (1999b) The influence of mineralogy on the initiation of microfractures in granite. In: Vouille G, Berest B (eds) 9th international congress on rock mechanics. A A Balkema, Rotterdam, pp 1007–1010
- Ewy RT, Cook NGW (1990) Deformation and fracture around cylindrical openings in rock—I. Observations and analysis of deformations. *Int J Rock Mech Min Sci Geomech Abstr* 27(5):387–407. doi:10.1016/0148-9062(90)92713-O
- Fuenkajorn K, Daemen JJK (1992) Drilling-induced fractures in borehole walls. *J Petrol Technol* 44(2):210–216. doi:10.2118/21301-PA
- Gaál G, Gorbatshev R (1987) An outline of the Precambrian evolution of the Baltic shield. *Precambrian Res* 35:15–52. doi:10.1016/0301-9268(87)90044-1

- Gay NC (1973) Fracture growth around openings in thick-walled cylinders of rock subjected to hydrostatic compression. *Int J Rock Mech Min Sci Geomech Abstr* 10(3):209–233. doi:10.1016/0148-9062(73)90032-6
- Haimson B (2007) Micromechanisms of borehole instability leading to breakouts in rocks. *Int J Rock Mech Min Sci* 44(2):157–173. doi:10.1016/j.ijrmms.2006.06.002
- Haimson BC, Herrick CG (1986) Borehole breakouts—a new tool for estimating in situ stress? In: Stephansson O (ed) Proceedings of international symposium on rock stress and rock stress measurements, Stockholm, pp 271–280
- Haimson BC, Herrick CG (1989) Borehole breakouts and in situ stress. In: Rowley JC (ed) Drilling symposium 1989, 12th annual energy-sources technology conference and exhibition, vol 22. ASME, New York, pp 17–22
- Hallbauer DK, Wagner H, Cook NGW (1973) Some observations concerning the microscopic and mechanical behaviour of quartzite specimens in stiff, triaxial compression tests. *Int J Rock Mech Min Sci Geomech Abstr* 10(6):713–726. doi:10.1016/0148-9062(73)90015-6
- Hardenby C, Sigurdsson O (2010) Äspö Hard Rock Laboratory. the TASS-tunnel, Geological mapping. SKB R-10-35, Swedish Nuclear Fuel and Waste Management Co., Stockholm
- HBM (2014) HBM test and measurement: transducers. Load cells, DAC. <http://www.hbm.com>
- Hoek E (1965) Rock fracture under static conditions. PhD thesis, Univ Cape Town, South Africa
- Jacobsson L, Christiansson R, Martin CD (2010) Experimental determination of rock spalling initiation in hard rock. In: Zhao J, Labiouse JP, Mathier JF (eds) Rock mechanics in civil and environmental engineering: European rock mechanics symposium EUROCK 2010. CRC Press, pp 327–330
- Kelsall PC, Case JB, Chanbannes CR (1982) Topical report. a preliminary evaluation of the rock mass disturbance resulting from shaft, tunnel and borehole excavation. Tech. Rep. Project No. NM79-137, D'Appolonia Consulting Engineers Inc., Albuquerque
- Kornfält KA, Persson PO, Wikman H (1997) Granitoids from the Äspö area, southeastern Sweden—geochemical and geochronological data. *GFF* 119:109–114. doi:10.1080/11035899709546465
- Kranz RL (1983) Microcracks in rocks: a review. *Tectonophysics* 100:449–480. doi:10.1016/0040-1951(83)90198-1
- Kronenberg AK, Kirby SH, Pinkston J (1990) Basal slip and mechanical anisotropy of biotite. *J Geophys Res Solid Earth* 95(B12):19257–19278. doi:10.1029/JB095iB12p19257
- Kyowa (2014) Strain-gage technologies kyowa. <http://www.kyowa-ei.com>
- Labuz JF, Dai ST, Papamichos E (1996) Plane-strain compression of rock-like materials. *Int J Rock Mech Min Sci Geomech Abstr* 33(6):573–584. doi:10.1016/0148-9062(96)00012-5
- Lajtai EZ (1972) Effect of tensile stress gradient on brittle fracture initiation. *Int J Rock Mech Min Sci Geomech Abstr* 9(5):569–578. doi:10.1016/0148-9062(72)90009-5
- Lajtai EZ (1998) Microscopic fracture processes in a granite. *Rock Mech Rock Eng* 31(4):237–250. doi:10.1007/s006030050023
- Li L, Lee P, Tsui Y, Tham L, Tang C (2003) Failure process of granite. *Int J Geomech* 3(1):84–98. doi:10.1061/(ASCE)1532-3641(2003)3:1(84)
- Lindqvist JE, Åkesson U, Malaga-Starzec K (2007) Microstructure and functional properties of rock materials. *Mater Charact* 58:1183–1188
- Liu S, Faisal Anwar AHM, Kim BC, Ichikawa Y (2006) Observation of microcracks in granite using a confocal laser scanning microscope. *Int J Rock Mech Min Sci* 43(8):1293–1305. doi:10.1016/j.ijrmms.2006.04.006
- Mahabadi OK (2012) Investigating the influence of micro-scale heterogeneity and microstructure on the failure and mechanical behaviour of geomaterials. PhD thesis, Univ. Toronto, Canada
- Martin CD (1993) The strength of massive Lac du Bonnet granite around circular underground openings. PhD thesis, University of Manitoba, Winnipeg
- Martin CD (1997) Seventeenth canadian geotechnical colloquium: the effect of cohesion loss and stress path on brittle rock strength. *Can Geotech J* 34(5):698–725. doi:10.1139/t97-030
- Martin CD, Christiansson R (2009) Estimating the potential for spalling around a deep nuclear waste repository in crystalline rock. *Int J Rock Mech Min Sci* 46(2):219–228. doi:10.1016/j.ijrmms.2008.03.001
- Martin CD, Martino JB, Dzik EJ (1994) Comparison of borehole breakouts from laboratory and field tests. In: EUROCK94, SPE/ISRM rock mechanics in petroleum engineering, pp 183–190
- Martin CD, Read RS, Martino JB (1997) Observations of brittle failure around a circular test tunnel. *Int J Rock Mech Min Sci* 34(7):1065–1073. doi:10.1016/S1365-1609(97)90200-8
- Mastin LG (1984) The development of borehole breakouts in sandstone. Master's thesis, Stanford University
- Myer LR, Kemeny JM, Zheng Z, Suarez R, Ewy RT, Cook NGW (1992) Extensile cracking in porous rock under differential compressive stress. *Appl Mech Rev* 45(8):263–280. doi:10.1115/1.3119758
- Nasseri M, Rezanezhad F, Young R (2011) Analysis of fracture damage zone in anisotropic granitic rock using 3D X-ray ct scanning techniques. *Int J Fract* 168(1):1–13. doi:10.1007/s10704-010-9551-0
- Nicksiar M, Martin CD (2012) Evaluation of methods for determining crack initiation in compression tests on low-porosity rocks. *Rock Mech Rock Eng* 45(4):607–617. doi:10.1007/s00603-012-0221-6
- Olsson M, Markström I, Pettersson A, Sträng M (2009) Examination of the excavation damaged zone in the TASS tunnel, Äspö HRL. SKB R-09-39, Swedish Nuclear Fuel and Waste Management Co., Stockholm
- Patchett PJ, Todt W, Gorbatshev R (1987) Origin of continental crust of 1.9–1.7 Ga age: Nd isotopes in the Svecofennian orogenic terrains of Sweden. *Precambrian Res* 35:145–160. doi:10.1016/0301-9268(87)90050-7
- Pinto C, Fonseca J (2013) Mechanical behavior of high strength granite for new prestressed stone structures. *Int J Rock Mech Min Sci* 60:452–460. doi:10.1016/j.ijrmms.2012.12.010
- Read RS (2004) 20 years of excavation response studies at aecl's underground research laboratory. *Int J Rock Mech Min Sci* 41(8):1251–1275. doi:10.1016/j.ijrmms.2004.09.012
- Read RS, Martin CD (1996) Technical summary of AECL's mine-by experiment. Phase 1: excavation response. Report AECL-11311, Atomic Energy of Canada Limited
- Seo YS, Jeong GC, Kim JS, Ichikawa Y (2002) Microscopic observation and contact stress analysis of granite under compression. *Eng Geol* 63:259–275. doi:10.1016/S0013-7952(01)00086-2
- Staub I, Andersson JC, Magnor B (2004) Äspö pillar stability experiment. Geology and mechanical properties of the rock in TASQ. SKB R-04-01, Swedish Nuclear Fuel and Waste Management Co., Stockholm
- Valley B, Evans KF (2005) Stress estimates from analysis of breakouts and drilling-induced tension fractures in GPK1 and GPK4. In: EHDRA scientific conference, vol 1
- Wahlgren CH, Ahl M, Sandahl KA, Berglund J, Petersson J, Ekström M, Persson PO (2004) Bedrock mapping 2003 - Simpevarp subarea. Outcrop data, fracture data, modal and geochemical classification of rock types, bedrock map, radiometric dating.

- Oskarshamn site investigation. SKB P-04-102, Swedish Nuclear Fuel and Waste Management Co., Stockholm
- Weed HC, Durham WB (1982) Drilling-induced borehole-wall damage at spent fuel test-climax. Tech. Rep. UCID-19672, U.S. DOE, Lawrence Livermore Laboratory, CA
- Wong TF (1982) Micromechanics of faulting in westerly granite. *Int J Rock Mech Min Sci Geomech Abstr* 19(2):49–64. doi:[10.1016/0148-9062\(82\)91631-X](https://doi.org/10.1016/0148-9062(82)91631-X)